Analytica Chimica Acta 1135 (2020) 73–82

Contents lists available at ScienceDirect

Analytica Chimica Acta

journal homepage: www.elsevier.com/locate/aca

Polycrystalline boron-doped diamond-based electrochemical biosensor for simultaneous detection of dopamine and melatonin

Zhen Yang [a], Mingji Li [a, *], Hongji Li [b, **], Huayi Li [a], Cuiping Li [a], Baohe Yang [a]

[a] Tianjin Key Laboratory of Film Electronic and Communication Devices, Engineering Research Center of Optoelectronic Devices & Communication Technology (Ministry of Education), School of Electrical and Electronic Engineering, Tianjin University of Technology, Tianjin 300384, PR China
[b] Tianjin Key Laboratory of Organic Solar Cells and Photochemical Conversion, Tianjin Key Laboratory of Drug Targeting and Bioimaging, School of Chemistry and Chemical Engineering, Tianjin University of Technology, Tianjin 300384, PR China

HIGHLIGHTS

- Moderately and heavily doped BDD films with high electrocatalytic activities are prepared.
- BDD electrode-based electrochemical biosensor is responsive to dopamine and melatonin.
- Moderately doped BDD shows selectivity owing to a variety and number of crystal planes.
- The biosensor exhibits a wide concentration range, low detection limit, and long service life.

GRAPHICAL ABSTRACT

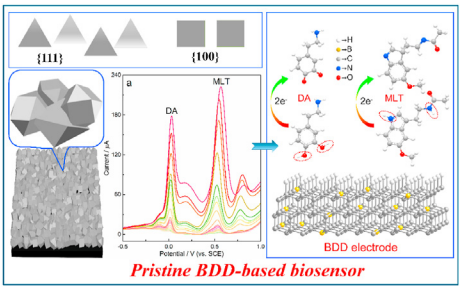

ARTICLE INFO

Article history:
Received 21 June 2020
Received in revised form
13 August 2020
Accepted 22 August 2020
Available online 27 August 2020

Keywords:
Boron-doped diamond
Boron content
Dopamine
Melatonin
Electrochemical biosensor

ABSTRACT

In this study, boron-doped diamond (BDD) electrodes with varied B contents are prepared to determine the feasibility of the direct usage of BDD as an electrochemical biosensor without any modification. The electrochemical performance of the electrodes was investigated through the characterization of electrochemical impedance spectroscopy for potassium ferricyanide/potassium ferrocyanide ($K_3Fe(CN)_6$/$K_4Fe(CN)_6$) redox couples, as well as through qualitative and quantitative analysis of the two biomolecules dopamine (DA) and melatonin (MLT). The results show that the B content of BDD is the primary parameter for controlling the electrocatalytic current, that is, the response sensitivity. However, the abundant crystal planes and low background current are the key factors in improving the selectivity of the biomarkers to identify multiple analytes. Considering the catalytic current and its ability to distinguish the biomolecules, BDD with a B source carrier gas flow rate of 18 sccm is used as the sensing electrode for the simultaneous detection of DA and MLT. The response peak potential difference reaches 500 mV, and the linear concentration range for the two analytes is 0.4–600 μM, with detection limits of 0.1 μM for DA and 0.003 μM for MLT. These results match those observed for electrochemical sensors modified by various sensitive materials. BDD electrodes show good chemical resistance, good stability, and no pollution and are suitable for long-term usage as biomarker sensors.

1. Introduction

Electrochemical (EC) biosensors have attracted significant interest because of their good selectivities, high sensitivities, fast

* Corresponding author.
** Corresponding author.
E-mail addresses: limingji@163.com, limingji@tjut.edu.cn (M. Li), hongjili@yeah.net, lihongji@tjut.edu.cn (H. Li).

https://doi.org/10.1016/j.aca.2020.08.042
0003-2670/

responses, and low cost [1]. The working electrodes of EC biosensors are typically constructed by using various electroactive materials as sensitive layers on the surfaces of glassy carbon [2], Au [3], Pt [4], and indium titanium oxide (ITO) [5] electrodes. Various biological materials [6], polymers [7], metals or metal oxides [8], and carbon materials [9] are designed with different nanoscale or porous structures containing high specific surface areas, which are attached to the current collector electrodes in a hybrid form to form sensitive layers. Common techniques for attaching these sensitive materials to the current collector electrodes include drop-coating [8], spin-coating [5], and electrodeposition [10]. However, because of the complexity of these processes, they are not suitable for application in industrial production. For industrial processes and realizing practical applications, a working electrode that can be used directly without any modification is desirable. Polycrystalline boron-doped diamond (BDD) films can meet this demand.

Polycrystalline BDD films show a wide range of applications in various EC fields, such as electrocatalytic oxidation for wastewater treatment [11,12], EC energy storage devices [13], and EC sensors [14,15]. The most important EC characteristics of BDD films include a low and stable background current, a wide potential window (in particular, a high O_2 overpotential), corrosion stability, self-cleaning ability, and a strong oxidation capacity [16–18]. Currently, BDD-based EC sensors including Ni/Cu/BDD for glucose detection [19], MCH/aptamers/Au-NPs/BDD for AFB_1 detection [20], Prussian blue-modified BDD for H_2O_2 detection [21], and nano-pyramid BDD for 4-nonylphenol detection [22] have been described in the literature. Previously, our research group reported BDD-based EC sensors, including amino acid sensors [23,24], organic compound sensors [25], tumor marker sensors [26], and other small biomolecule sensors [27,28]. Simultaneously, other studies were directed toward the surface modification and development of composite technology for BDD films, including etching into the porous structure [27], electrodeposited nickel-nickel oxide nanostructure [23], and graphene growth on the BDD surface [26]. These results showed that the BDD electrodes significantly increased the response current of the analyte and were suitable as current collectors for working electrodes.

BDD electrodes with varied B-doping content show different binding energies and carrier densities in terms of semiconductor applications. These properties significantly affect the current and oxidation peak potential of the analyte, which influence the analyte detection performance [29]. Recently, we systematically analyzed the effect of B-doping content on the morphology, composition, and EC performance of BDD films [25]. With a high B-doping content in BDD, a significant electrocatalytic effect was observed on the organic molecules, affording non-unique oxidation products of the organic molecules and even direct decomposition. This decreased the production of specific oxidation products and led to a decrease in the catalytic current. In contrast, when the B-doping level was moderate, the oxidation products of organic molecules were unique, and the peak current of a specific redox couple was high. Additionally, it has been reported that the different crystal planes of BDD show variations in electrocatalytic activity due to different effective surface areas [30]. Varying B contents in various crystal planes of BDD lead to differences in the material composition, leading to different electrical and EC properties. For example, the electrical conductivity is enhanced with increased B-doping because of the high density of the electronic states formed on the BDD film [31]; the B-doping level also affects the Faradaic efficiency for generating different products [32]. Therefore, it is speculated that a BDD film with an appropriate B content shows the electrical properties of a qualified current collector, possessing numerous crystal planes with different doping levels. This can expose abundant crystal surfaces with different electrocatalytic activities in the electrolyte and can electrocatalyze various analytes, allowing direct distinction between various biomolecules without modification and trace detection.

In this study, six types of polycrystalline BDD electrodes with significantly different B-doping content were prepared, and the effects of B doping amount on the grain sizes, B doping states, and EC performances of the BDD films were investigated. Under optimized conditions, the electrical analysis of dopamine (DA) and melatonin (MLT) was systematically conducted. Finally, an EC biosensor that is simultaneously responsive to DA and MLT was constructed, and a quantitative detection model suitable for serum analysis is proposed. As DA and MLT are neurotransmitters, the simultaneous detection of these analytes is important for investigating neurodegenerative diseases such as cerebral ischemia, brain injuries, Alzheimer's disease, and Parkinson's disease, and for improving physiological functions such as sleep [33–35].

2. Experimental

2.1. Chemicals and materials

DA hydrochloride, serotonin, and uric acid were purchased from Alfa Aesar (Haverhill, MA, USA). $K_3Fe(CN)_6$, $K_4Fe(CN)_6$, KCl, and NaOH were obtained from Tianjin Fengchuan Chemical Reagent Technology Co., Ltd. (Tianjin, China). Na_2HPO_4, NaH_2PO_4, L-Lysine, L-cysteine, and pyridoxine were purchased from the Tianjin Guangfu Fine Chemical Industry Research Institute (Tianjin, China). MLT, thymine, ascorbic acid, and guanine were procured from Shanghai Yuanye Bio-Technology Co., Ltd. (Shanghai, China). KCl, tryptophan, H_3PO_4, and glucose were purchased from the Tianjin Damao Chemical Reagent Factory (Tianjin, China). Human serum was obtained from Solarbio Life Science (Beijing, China), and trimethyl borate ($B(OCH_3)_3$) was purchased from Shanghai Macklin Biochemical Technology Co., Ltd. (Shanghai, China). All chemicals were of analytical grade and used as received without further purification. Phosphate buffered saline (PBS) solutions as supporting electrolytes were prepared by mixing 0.1 M Na_2HPO_4, 0.1 M NaH_2PO_4, 0.1 M H_3PO_4, and 0.1 M NaOH with 18 MΩ ultrapure water. The pH of the supporting electrolyte was controlled using a PHS-3C pH meter (Shanghai INESA Scientific Instrument Co., Ltd., Shanghai, China).

2.2. Preparation of BDD electrodes

Six types of polycrystalline BDD films with different B contents were deposited onto a $20 \times 10 \times 1$ mm^3 Ta substrate (99.99% purity) using an electron-assisted hot filament chemical vapor deposition (EA-HFCVD) system. The chemical vapor deposition (CVD) system was equipped with three gas paths for introducing the carbon source (methane, CH_4), H_2, and additional H_2 gas as a source carrier for B. A liquid B source, which was a mixture of trimethyl borate ($B(OCH_3)_3$) and ethanol with a volume ratio of 3:1, was introduced into the reaction chamber by bubbling H_2 gas, which was known as the B-source H_2. The flow rates of CH_4 and H_2 were maintained at 6 sccm and 300 sccm, respectively. The flow rates of B-source H_2 were set to 3, 16, 18, 20, 24, 27, and 36 sccm, which corresponded to samples termed 3-BDD, 16-BDD, 18-BDD, 20-BDD, 24-BDD, 27-BDD, and 36-BDD, respectively. The pressure of the reaction chamber was controlled at 5000 Pa. In addition, a DC electric field with a bias voltage of 200 V and bias current of 10 A was applied between the hot filament and substrate. The substrate temperature was controlled at approximately 950 °C with continuous deposition for 8 h followed by natural cooling to obtain the various BDD films.

2.3. Characterization

The morphologies of the surfaces and cross-sections of the BDD films were characterized using field-emission scanning electron microscopy (FE-SEM, MERLIN Compact, Carl Zeiss, Oberkochen, Germany). The phase structures and compositions of different BDD electrodes were characterized using Raman spectroscopy (LabRAM HR Evolution, HORIBA Scientific, Kyoto, Japan; YAG laser with 532 nm wavelength) and X-ray diffraction (XRD) (D/Max 2500/PC, Rigaku Corporation, Tokyo, Japan). The EC performance was investigated by employing electrochemical impedance spectroscopy (EIS) analysis in conjunction with differential pulse voltammogram (DPV), square wave voltammetry (SWV), chronoamperometric responses (i-t), and cyclic voltammogram (CV) data, using a CHI 760E EC workstation (Shanghai CH Instrument Company, Shanghai, China). The three-electrode system was composed of a BDD working electrode, Pt auxiliary electrode, and a saturated calomel electrode as the reference electrode. Square wave voltammetry (SWV) curves were recorded from −0.6 to 1.2 V by applying a positive scan with a potential step increment of 4 mV, amplitude of 25 mV, frequency of 15 Hz, and quiet time of 2.0 s. The chronoamperometric response (i-t) curve measurements were recorded at a specific potential during constant stirring of 0.1 M PBS (pH 7.0). The geometric area of the BDD electrode immersed in the electrolyte was 1 cm^2, and the distance between the electrodes was 1 cm.

3. Results and discussion

3.1. Design strategy of BDD-based sensors

Fig. 1 shows the design strategy of the BDD-based biosensor. The differences in the inherent electrical and EC properties of the polycrystalline BDD electrodes determined the conditions employed to distinguish and quantitatively analyze DA and MLT. A high B-doping content increases the carrier concentration of the BDD film, which is important for charge transfer in the diamond lattice [29], thereby increasing the efficiency of converting the ionic current into electronic current as a polarized electrode. In contrast, a BDD electrode with an appropriate B-doping level can possess both a low background current and suitable electrocatalytic activity. For the BDDs with an identical geometric area, the crystals are small and numerous, such that a large number of crystal planes of various types are exposed on the surface. For the EC sensors that are responsive to multiple analytes, their sensitivity is directly related to the catalytic current, while the selectivity is related to the background current and response potential of the analyte. The B-doping level also affects the flat-band potential that can reflect the oxidation peak potential [29]. Graphite carbon impurities were etched with an oxygen-containing liquid B-source ($B(OCH_3)_3$) to prepare the BDD films with clear grain boundaries and varied B-doping content. The samples could be classified into small crystals and moderately doped BDD films, as well as large crystals and heavily doped BDD films. The method for the simultaneous detection of DA and MLT was developed using these BDD electrodes.

3.2. Morphological and topographic characterization of BDD electrodes

Fig. 2 shows the SEM images of the BDD films with B-source H_2 flow rates of 3, 16, 18, 20, 27, and 36 sccm. The crystal size of BDD increased gradually with an increase in the B content. Furthermore, the B-source H_2 flow rate was 18 sccm at the critical point of crystal growth; 3-BDD, 16-BDD, and 18-BDD contained small-sized crystals; and 20-BDD, 27-BDD, and 36-BDD contained large-sized crystals. Specifically, when the B-source H_2 flow rate was 18 sccm, the diamond crystals were in the range of 2–5 μm. However, when the B-source H_2 flow rate was 36 sccm, the crystal size was 5–10 μm. In addition, the thicknesses of various BDD films were different, but all exceeded 5 μm (insets). As shown in Fig. 2b and d, when the flow rate ratio of B-source H_2 for 36-BDD and 18-BDD was 2:1, the lattice distortion effect caused by B-doping was significantly different. As observed in Fig. 2d, the lattice distortion of the (111) lattice face of BDD was very severe, such that even the traces for the layered exfoliation of the crystal plane can be observed.

Fig. 3(a and b) show the Raman spectra of {111} and {100} planes of the six BDD films. In the Raman spectra of the six BDD films, the sp^3 C–C diamond peak was observed at 1315–1337 cm^{-1}, but the intensity of the peak gradually decreased with an increase in the B

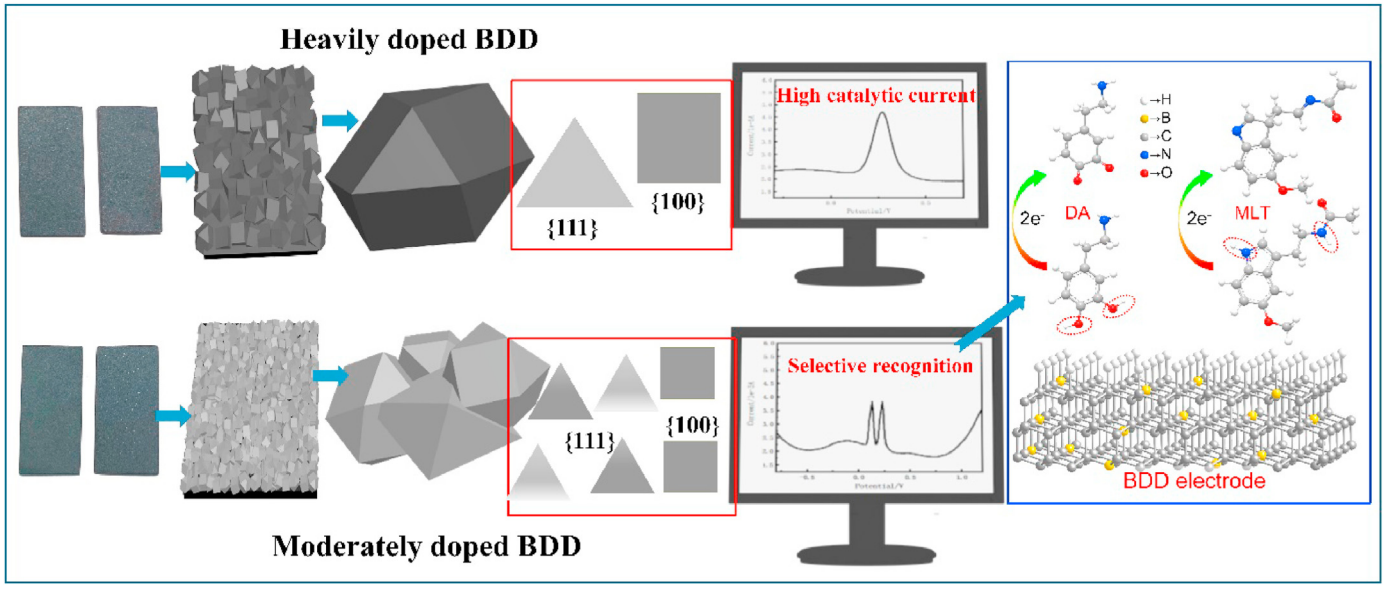

Fig. 1. Schematic of the pristine B-doped diamond (BDD)-based biosensor.

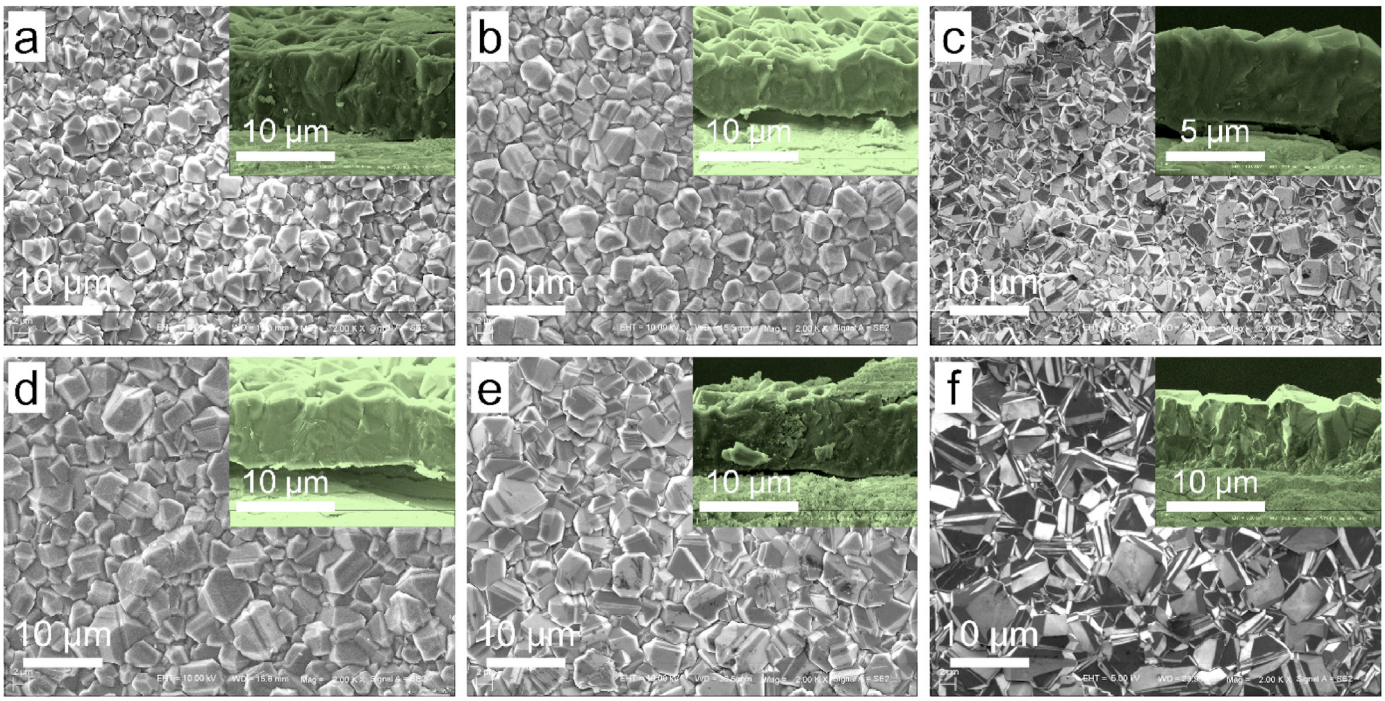

Fig. 2. Scanning electron microscopy (SEM) images of BDD films with B-source H_2 gas flow rates of (a) 3, (b) 16, (c) 18, (d) 20, (e) 27, and (f) 36 sccm. Insets show the cross-sectional SEM images of the BDD films.

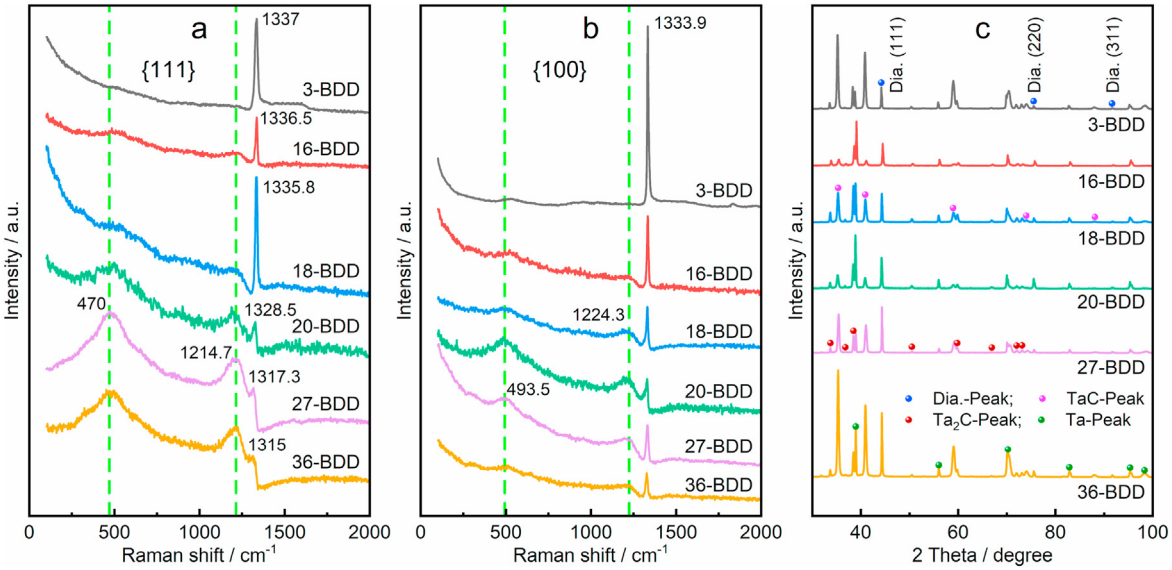

Fig. 3. Raman spectra of the (a) {111} and (b) {100} planes of BDD films. (c) X-ray diffraction patterns of BDD films.

content [30,36]. In addition, the diamond peak appeared to be asymmetric and shifted to a low wavenumber with an increase in the B content, which is related to the tensile stress and Fano resonance phenomenon caused by the B atoms [37,38]. Furthermore, the broad bands at approximately 480 cm^{-1} and 1215 cm^{-1} increased gradually; these are related to the B–B bond and B–C vibration, respectively, in the diamond lattice [32]. These bands were typically observed for the 27-BDD and 36-BDD electrodes. The B content in the {111} plane was higher than that in the {100} plane. The heavily doped BDD had a large crystal size, while the BDD with a low B-content contained numerous small crystals.

Based on the XRD patterns of the six BDDs, the characteristic peaks of the (111), (220), and (311) planes of diamond can be observed at diffraction angles of 44.5°, 75.8°, and 91.8°, respectively (Fig. 3b; JCPDS 65–0537) [11]. The characteristic peaks of the Ta substrate and tantalum carbide (TaC and Ta_2C) transition layer are also apparent in all XRD patterns.

3.3. EC characterization of BDD electrodes

Fig. 4(a and b) show the Nyquist plots of the 3-BDD, 16-BDD, 18-BDD, 20-BDD, 27-BDD, and 36-BDD electrodes. The equivalent

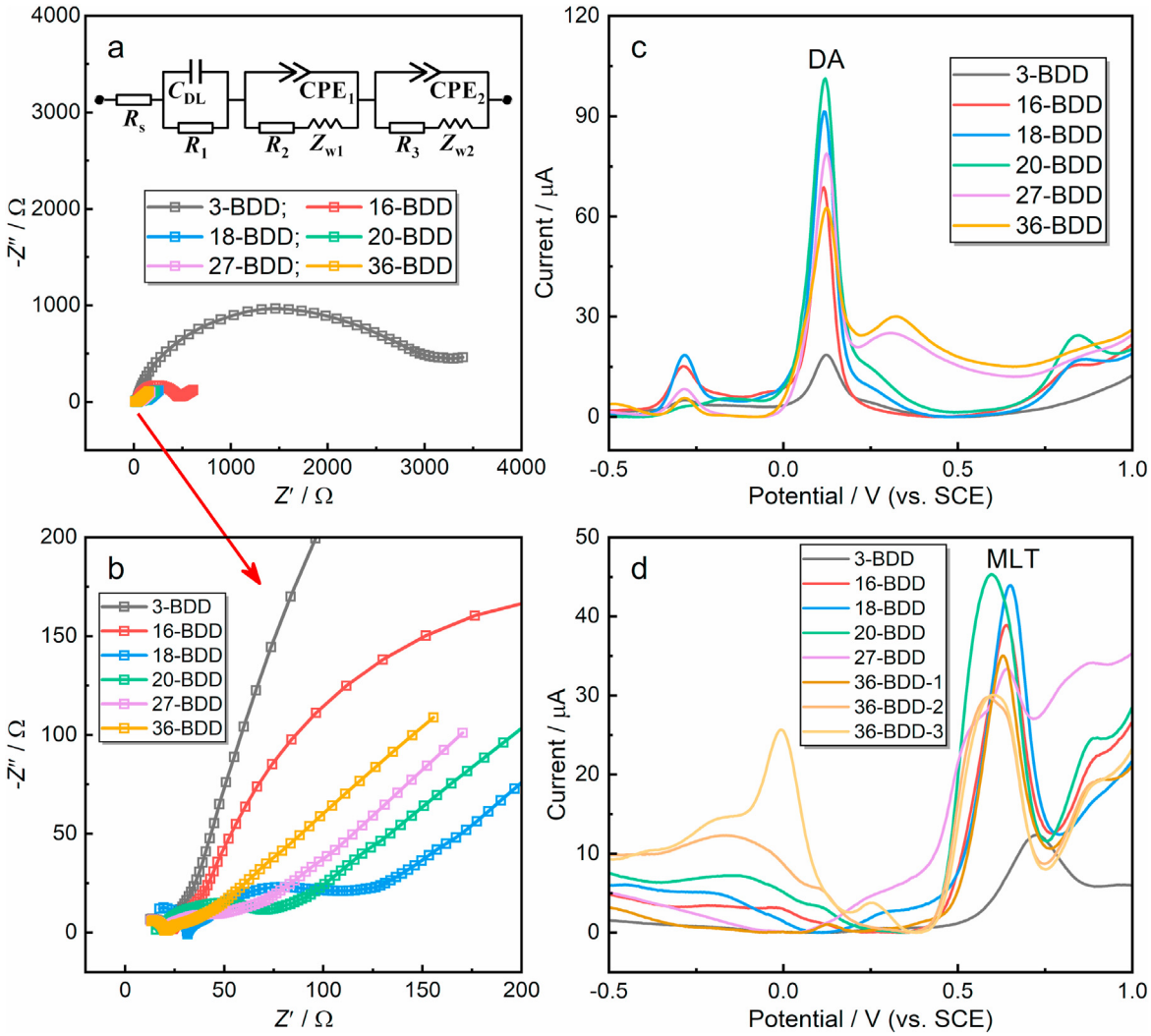

Fig. 4. (a) Nyquist plots of 3-BDD, 16-BDD, 18-BDD, 20-BDD, 27-BDD, and 36-BDD films in the frequency range of 0.01–100 kHz. The inset shows the equivalent circuit. (b) High-frequency region of the amplified Nyquist plots. The electrolyte is a 0.1 M KCl solution containing 5 mM $K_3Fe(CN)_6$ and 5 mM $K_4Fe(CN)_6$) redox couples. (c, d) Differential pulse voltammogram (DPV) curves of 3-BDD, 16-BDD, 18-BDD, 20-BDD, 27-BDD, and 36-BDD electrodes recorded in (c) 0.1 mM dopamine (DA) and (d) 50 μM melatonin (MLT). The supporting electrolyte is PBS (pH 7.0, 0.1 M).

circuit was designed based on the non-negligible resistances of the electrolyte (R_s), liquid–solid interface (electrolyte-BDD, R_1), solid (BDD, R_2), and solid–solid interface (BDD-Ta, R_3), as shown in the inset of Fig. 4a. For the sensor electrode, the charge transfer resistance (R_1) of the liquid–solid interface between the electrolyte and electrode, as well as the ion-transfer kinetic process in the electrolytic cell were the main factors affecting the polarization current. The R_1 value decreased gradually with an increase in the B content (1382, 284.90, 24.61, 16.63, 12.34, and 12.76 Ω cm^{-2}), which is correlated to an increase in the electron mobility of the BDD film. In addition, when the flow rate of the B source was 18 sccm, a straight line was obtained in the Nyquist plot of the 18-BDD electrode, which indicates that the ion-diffusion process plays an important role.

The DPV curves were recorded in a 0.1 mM DA solution using these six BDD electrodes (Fig. 4c). The peak current of DA increased when the B-source H_2 flow rate increased from 3 to 20 sccm. However, the oxidation peak of DA broadened when the B-source H_2 flow rate increased to 20 sccm. When 27-BDD and 36-BDD were used to detect DA, the DA peak was superimposed with a large shoulder, which clearly reduced the discrimination capability of the multi-target response. The DPV curves were also obtained in the MLT solution using the six BDD electrodes (Fig. 4d). The main oxidation peak of MLT is located at approximately 0.65 V, but the oxidation current of MLT appeared at approximately −0.1 V. The oxidation current at about −0.1 V increased with the increase of B content and became a sharp peak during continuous oxidation. For the simultaneous detection of DA and MLT, the oxidation current of the MLT may have interfered with the response current of DA. Furthermore, the oxidation current of MLT at −0.1 V increased with increasing MLT concentration, which can be observed in subsequent investigations (Fig. 6b). Considering its resulting resolution of DA and MLT and its high response current signal, the 18-BDD electrode was selected to systematically construct an EC sensor for the simultaneous detection of DA and MLT.

3.4. Optimization of pH value

Fig. 5(a and b) show the DPV curves recorded twice in a mixed solution of 80 μM DA and 200 μM MLT using the 18-BDD electrode. The peak currents of DA recorded in the second pass were significantly lower than those recorded in the first pass. This indicates

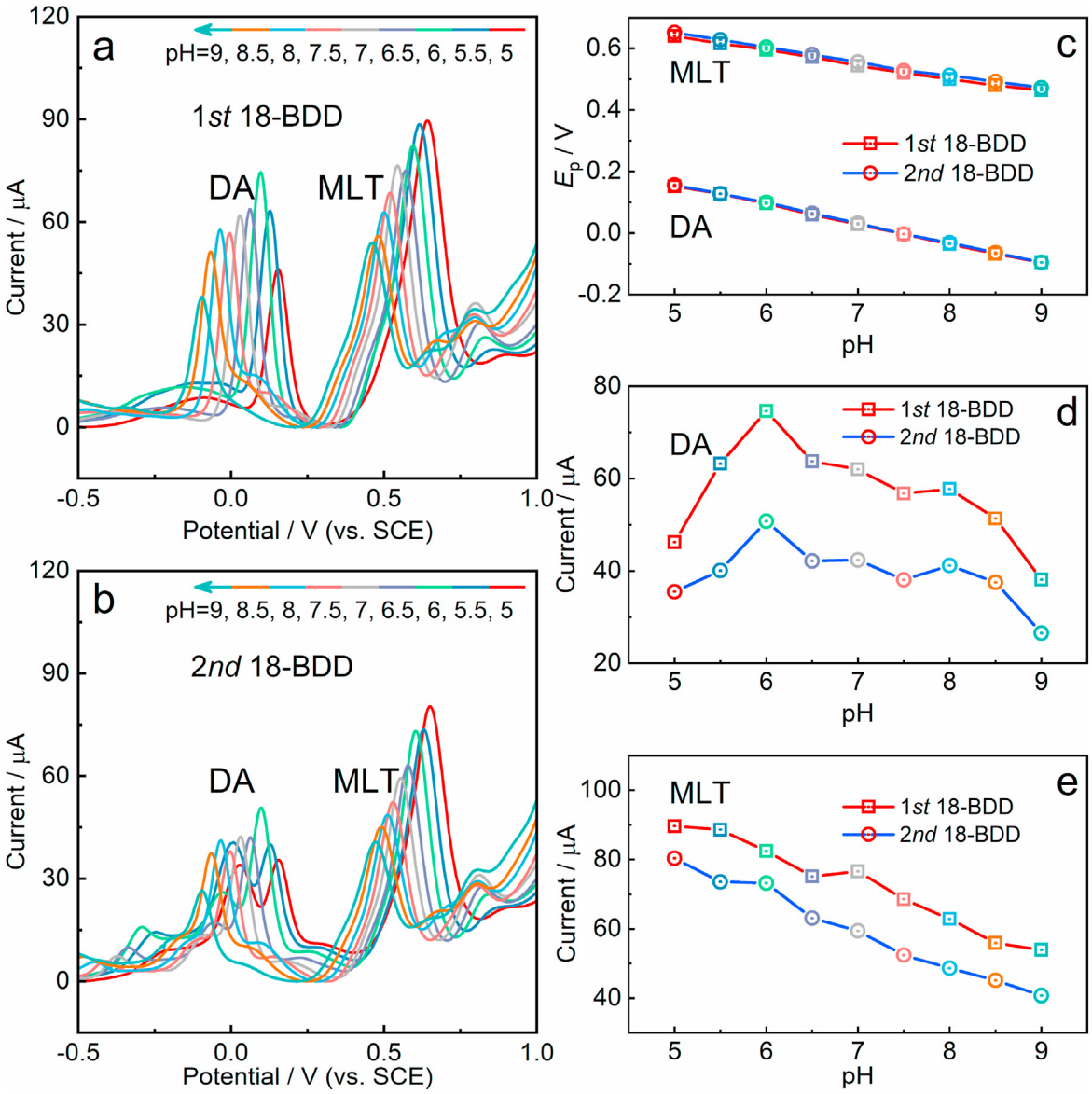

Fig. 5. (a, b) DPV curves for 18-BDD electrode in 0.1 M PBS containing 80 μM DA and 200 μM MLT at different pH values (pH 5–9). (c) Calibration plots of peak potential versus the pH value. (d, e) Plots of peak current versus the pH value.

that the BDD electrodes rapidly and electrocatalytically oxidized DA. For the DPV curves recorded twice in succession, the peak potentials of DA and MLT remained almost unchanged. It can be observed that in the mixture of DA and MLT, the qualitative response signals, that is, the peak potentials, of the 18-BDD electrode to both compounds were stable. However, the peak potentials of DA and MLT shifted toward the negative potential with an increase in pH. This indicates that the protons (H^+) were involved in the EC reaction of DA and MLT. Furthermore, the electrode potentials of the two redox probes (DA and MLT) decreased as the pH value increased, by utilizing the Nernst equation ($E_P = E^\theta - \frac{2.303RT}{nF}pH + \frac{2.303RT}{nF}\log\left(\frac{[DA_{ox}]}{[DA_{red}]}\right)$) [39–41]. Here, E_P is the electrode potential, E^θ is the standard potential, R is the universal gas constant, T is the absolute temperature, n is the number of electrons, and F is Faraday's constant.

A linear relationship is observed between the peak potentials of DA and MLT and the pH value, such that the data were fitted and linear regression equations were established (Fig. 5c). The average slopes of the linear equations for DA and MLT are 63 mV pH^{-1} and 45 mV pH^{-1}, respectively. According to the Nernst equation, when the numbers of proton and electron transfers in a redox reaction are identical, a pH value causes a theoretical potential change of 59 mV. Therefore, by combining the molecular structures of DA and MLT, it can be observed that DA and MLT underwent an EC reaction that transferred two electrons and two protons on the BDD electrode surface (Fig. 1).

Fig. 5(d and e) show the plots depicting the relationship between pH and peak current. The peak current of MLT decreased almost linearly with an increase in the pH value, and its response signal was significantly high under acidic conditions. However, the response current of DA shows a maximum value at pH 7. A quantitative analysis was conducted using an electrolyte with pH 7.0, because the response current of DA was high, and human serum is neutral.

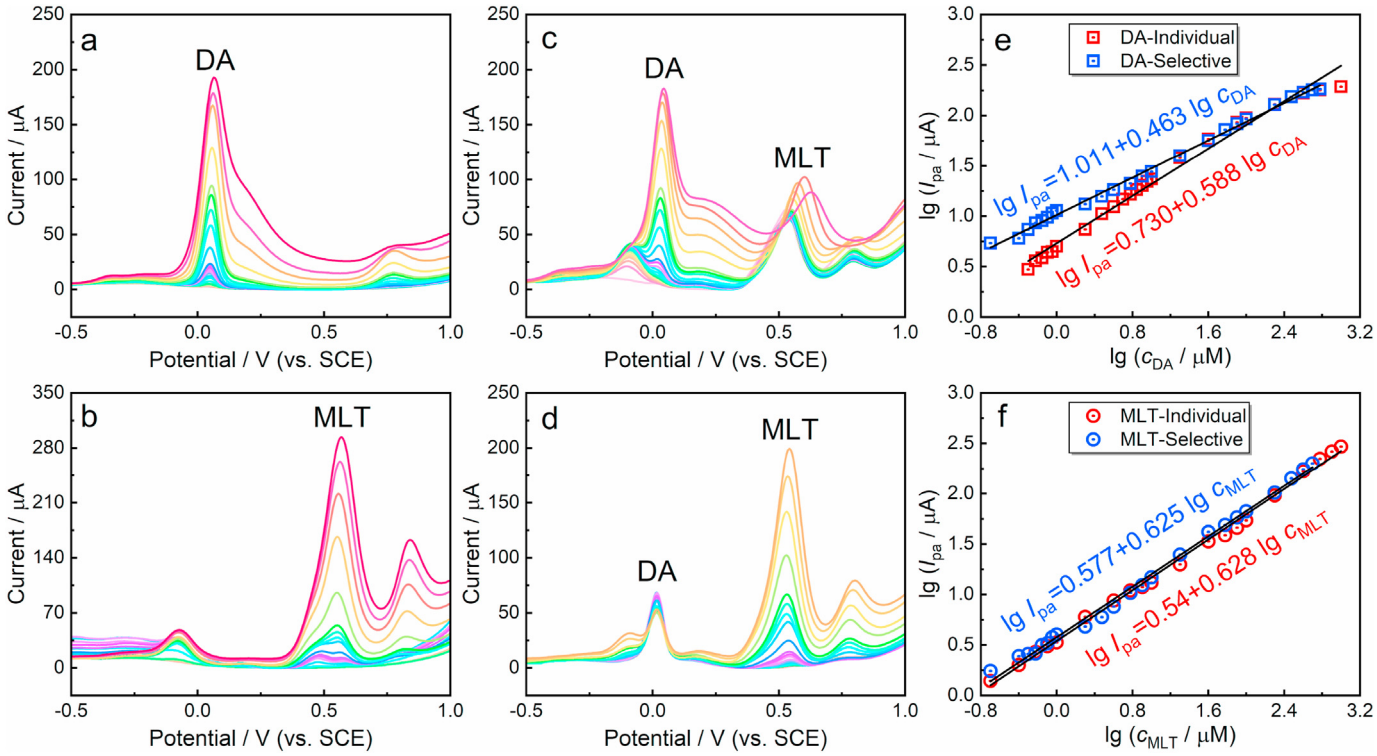

Fig. 6. (a–d) DPV and (e, f) regression curves for the individual and selective detection of DA and MLT using the 18-BDD electrode in (a) different concentrations of DA, (b) different concentrations of MLT, (c) different concentrations of DA and 120 μM MLT, and (d) 42 μM DA and different concentrations of MLT. (e, f) Plots of the oxidation peak current versus the concentration of each analyte.

3.5. Analytical performance of BDD electrode

Fig. 6(a–d) show the DPV curves for different concentrations of DA or MLT standard solutions obtained using the 18-BDD electrode. The peak currents of DA and MLT gradually increased as their respective concentrations increased. Additionally, irrespective of the co-existence of MLT with a specific concentration in the DA standard solution or a specific concentration of DA in the MLT solution, the peak current of the coexisting analyte was not significantly affected by a change in the concentration of the other substance and can therefore be neglected. Fig. 6e and f shows the dependence of the concentrations of DA and MLT, respectively, on their corresponding peak currents. A logarithmic method was used to establish a linear regression equation between the concentration and peak current because the range of the analyte concentration varied by up to four orders of magnitude (10^{-7}–10^{-4} mol L^{-1}).

Thereafter, a mixture of the two analytes was prepared by changing the concentrations of DA and MLT, and a series of DPV curves were obtained (Fig. 7a). The peak currents increased with an increase in the concentrations of DA and MLT, and a linear dependence is observed between the logarithm of the concentration and peak current (Fig. 7(b and c)). Table 1 includes the data for the linear concentration ranges, linear regression equations, and linear correlation coefficients (R) for individual, selective, and simultaneous detections. For each type of detection of DA and MLT, the slope of the regression equation corresponds to the sensitivity of the BDD sensing electrode. Under the above three detection conditions, the standard deviations for the sensitivities of the BDD sensor electrode to DA and MLT were 5.1% and 0.4%, respectively, both of which are <10% of the recognized error of the instrument. The result indicates that the 18-BDD electrode-based biosensor allows an accurate and quantitative analysis of DA and MLT. In general, for the simultaneous detection of DA and MLT, the linear concentration range of the EC biosensor was 0.4–600 μM, sensitivities were 0.521 lg (μA $μM^{-1}$) and 0.634 lg (μA $μM^{-1}$), and low limits of detection (LOD) were 0.1 μM and 0.003 μM, respectively. In addition, we used SWV and i-t methods to further verify the quantitative response of the 18-BDD electrode to DA and MLT (Fig. 7(d–h)). For the SWV method, the linear concentration ranges were 0.2–600 μM for DA and 0.4–1000 μM for MLT; when using the i-t method, the linear ranges were 0.3–583 μM for DA and 0.3–778 μM for MLT. Under the two EC methods of SWV and i-t, the 18-BDD electrode exhibited a linear concentration range close to or even wider than that of the DPV method. Evidently, the sensitivity and LOD of the detection results were different owing to the different excitation waveforms applied by the three EC methods. Nevertheless, compared with the other reported EC sensors (Table 2), the BDD-based biosensor affords a low LOD and wide linear ranges for the detection of DA and MLT [14,33,42–48].

3.6. Determination of DA and MLT in human serum

To verify its capability to analyze real samples, the BDD electrode was employed for the analysis of DA and MLT in human serum; the data are listed in Table S1. In the table, 0.19 μM of DA and 0.09 μM of MLT were detected in 20% serum. The recoveries of the four spikes were 96.5–104.7% and 95.6–102.9% for DA and MLT, respectively. These results indicate the accuracy of the biosensor in determining the DA and MLT content in real samples.

3.7. Selective determination of DA and MLT in the presence of interfering compounds using the BDD electrode

The interference mitigation capability of the BDD electrode for

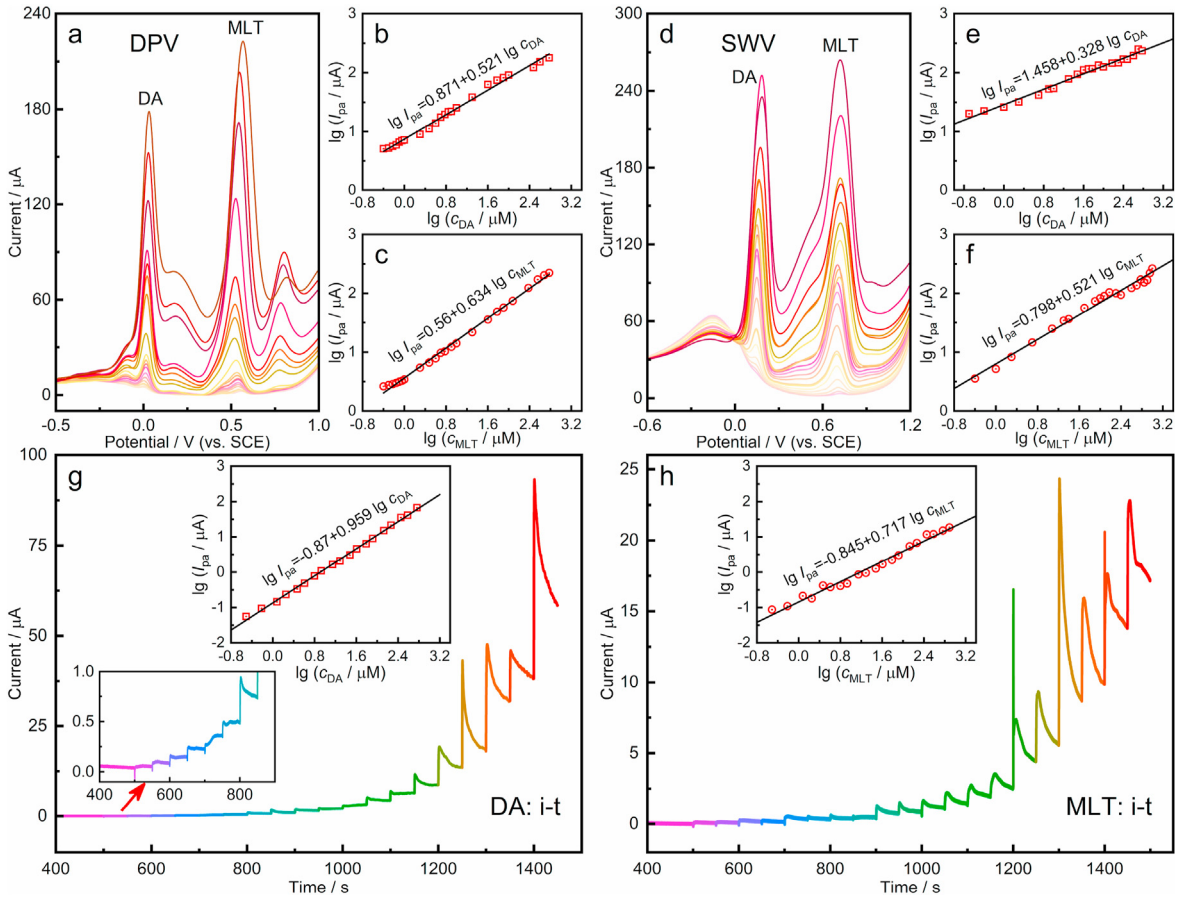

Fig. 7. Quantitative analysis of DA and MLT using the 18-BDD electrode with different electrochemical methods. (a) DPV curves at varying concentrations of DA and MLT, and (b,c) the corresponding plots of the oxidation peak current versus the DA or MLT concentration. (d) SWV curves and (e, f) the corresponding calibration curves. (g) Amperometric responses to the successive addition of DA into a 0.1 M PBS solution at 0.2 V. (h) Amperometric responses to the successive addition of MLT into a 0.1 M PBS solution at 0.6 V. The illustrations in (g) and (h) depict the calibration curves.

Table 1
Linear concentration ranges, regression equations, and correlation coefficients for the individual, selective, and simultaneous detections of DA and MLT.

Detection Method	Linear concentration range (μM)		Regression equation (μA, μM)		Correlation coefficient	
	DA	MLT	DA	MLT	DA	MLT
Individual	0.5–1000	0.2–1000	$\lg I_{pa} = 0.730 + 0.588 \lg c_{DA}$	$\lg I_{pa} = 0.540 + 0.628 \lg c_{MLT}$	0.985	0.996
Selective	0.2–600	0.2–500	$\lg I_{pa} = 1.011 + 0.463 \lg c_{DA}$	$\lg I_{pa} = 0.577 + 0.625 \lg c_{MLT}$	0.996	0.995
Simultaneous	0.4–600	0.4–600	$\lg I_{pa} = 0.871 + 0.521 \lg c_{DA}$	$\lg I_{pa} = 0.560 + 0.634 \lg c_{MLT}$	0.992	0.998

Table 2
Comparison of the performance indicators of different EC sensors for detecting DA and MLT.

Sensor	Concentration range/μM		Limit of detection/μM		Ref.
	DA	MLT	DA	MLT	
Au/porous BDD	0.1–1000	–	0.06	–	[14]
Au–MoS_2/GCE	–	0.033–10	–	0.0157	[33]
$K_2Fe_4O_7$/GCE	1–140	–	0.22	–	[42]
2, 6 DAP-ERGO/MoO_3	0.1–900	–	0.025	–	[43]
BDD	0.1–200	–	0.0187	–	[44]
PdNP@Al_2O_3/CPE	0.05–1450	0.006–1400	0.0365	0.0216	[45]
BDD-nanoelectrode arrays	0.1–20	–	0.1	–	[46]
SnO_2–Co_3O_4@rGO/IL/CPE	–	0.02–6	–	0.0041	[47]
PdNPs:ErGO/GCE	–	5–100	–	0.09	[48]
18-BDD/Ta	0.4–600	0.4–600	0.1	0.003	This work

the detection of DA and MLT in the presence of various compounds (0–200 μM guanine, 0–5000 μM glucose, 0–800 μM L-lysine, 0–1000 μM thymine, 0–1000 μM uric acid, 0–200 μM pyridoxine, 0–400 μM L-cysteine, 0–500 μM L-tryptophan, 0–400 μM L-ascorbic acid, and 0–80 μM serotonin) was investigated by employing the DPV method. In the DPV data (Fig. S1), no significant changes in the peak currents are observed for the above interferents. Interestingly, the 18-BDD sensor electrode was responsive toward L-cysteine, L-tryptophan, L-ascorbic acid, and serotonin, in addition to DA and MLT, with peak potentials at approximately 0.43, 0.73, −0.02, and 0.26 V, respectively (Fig. S2). Therefore, the 18-BDD electrode is a promising candidate for the analysis of DA and MLT molecules, showing no significant effects of interferences from other compounds.

3.8. Repeatability and stability of the BDD electrode

The operational stability of the 18-BDD electrode was determined by recording the CVs of the mixture containing 100 μM DA and 240 μM MLT in 0.1 M PBS (pH 7.0) at a scan rate of 100 mV s^{-1} for 100 cycles (Fig. S3). The BDD electrode retained approximately 95% and 92% (after 100 cycles) of its initial current during the oxidation of DA and MLT, respectively. In addition, the 18-BDD electrode was used to record the DPV curves in the mixed solutions of DA and MLT (five solutions), which are shown in Fig. S4. The results show that the repeated testing of five mixed solutions of DA and MLT with equal concentrations did not significantly decrease the peak current response of the electrode. Approximately 96.2% and 93% of the initial current responses to DA and MLT oxidation were retained, indicating that the BDD electrode shows good operational stability.

Three BDD electrodes produced using different durations were selected to verify the long-term stability. The usage frequency of these electrodes was >1000 times. These were used to record the DPV curves for the individual, selective, and simultaneous quantitative models. A series of DPV curves were obtained in a mixed solution of 40 μM DA and 40 μM MLT (Fig. S5). Among the three 18-BDD electrodes, two electrodes had a production time of approximately 2 years and one electrode took 6 months to produce. Compared with the DPV curves originally obtained under the same conditions, the peak potentials of DA and MLT in these DPV curves did not change significantly, and the decrease in the peak current was <15%. These results confirm that the BDD electrode exhibits a long-term stable EC performance.

4. Conclusions

BDD electrodes with varied B-doping content were prepared using the EA-HFCVD method. Heavily doped BDD films with large crystals and moderately doped BDD films with small crystals were prepared using the etching effect of an oxygen-containing B-source on graphite carbon impurities. The 18-BDD electrode was used as the sensing electrode to construct a three-electrode biosensor to simultaneously detect DA and MLT. The B-doped BDD electrode with a B-source H_2 gas flow rate of 18 sccm affords a high response current and excellent selectivity for DA and MLT. Furthermore, this electrode shows an appropriate electrocatalytic effect due to moderate B-doping; the number of exposed crystal planes is large owing to the relatively small crystal size, and the different doping levels of these crystal planes promote an abundant number of active sites. The biosensor shows a wide linear range (0.4–600 μM for DA and MLT), a low detection limit (0.1 μM for DA and 0.003 μM for MLT), and good storage capability, affording desirable results for the simultaneous determination of DA and MLT in serum samples, which can be useful for practical applications in clinical diagnostics.

CRediT authorship contribution statement

Zhen Yang: Conceptualization, Methodology. **Mingji Li:** Writing – review & editing, Funding acquisition, Supervision. **Hongji Li:** Investigation, Data curation, Writing - original draft, preparation. **Huayi Li:** Software. **Cuiping Li:** Formal analysis. **Baohe Yang:** Supervision.

Declaration of competing interest

The authors declare that they have no known competing financial interests or personal relationships that could have appeared to influence the work reported in this paper.

Acknowledgments

This work was supported by the Key Realm R&D Program of Guangdong Province, China (Grant No. 2019B020219002) and the Natural Science Foundation of Tianjin City (Grant Nos. 17JCZDJC32600 and 17JCQNJC00900).

Appendix A. Supplementary data

Supplementary data to this article can be found online at https://doi.org/10.1016/j.aca.2020.08.042.

References

[1] E. Cesewski, B.N. Johnson, Electrochemical biosensors for pathogen detection, Biosens. Bioelectron. 159 (2020) 112214.
[2] W. Liu, Q. Shi, G. Zheng, J. Zhou, M. Chen, Electrocatalytic oxidation toward dopamine and acetaminophen based on AuNPs@TCnA/GN modified glassy carbon electrode, Anal. Chim. Acta 1075 (2019) 81–90.
[3] A. Kurniawan, F. Kurniawan, F. Gunawan, S.-H. Chou, M.-J. Wang, Disposable electrochemical sensor based on copper-electrodeposited screen-printed gold electrode and its application in sensing l-Cysteine, Electrochim. Acta 293 (2019) 318–327.
[4] G.C.M.d. Oliveira, J.H.d.S. Carvalho, L.C. Brazaca, N.C.S. Vieira, B.C. Janegitz, Flexible platinum electrodes as electrochemical sensor and immunosensor for Parkinson's disease biomarkers, Biosens. Bioelectron. 152 (2020) 112016.
[5] S. Taniselass, M.K.M. Arshad, S.C.B. Gopinath, Graphene-based electrochemical biosensors for monitoring noncommunicable disease biomarkers, Biosens. Bioelectron. 130 (2019) 276–292.
[6] H. Que, D. Zhang, B. Guo, T. Wang, H. Wu, D. Han, Y. Yan, Label-free and ultrasensitive electrochemical biosensor for the detection of EBV-related DNA based on AgDNCs@DNA/AgNCs nanocomposites and lambda exonuclease-assisted target recycling, Biosens. Bioelectron. 143 (2019) 111610.
[7] K. Spychalska, D. Zajac, J. Cabaj, Electrochemical biosensor for detection of 17 beta-estradiol using semi-conducting polymer and horseradish peroxidase, RSC Adv. 10 (2020) 9079–9087.
[8] S.H. Baek, J. Roh, C.Y. Park, M.W. Kim, R. Shi, S.K. Kailasa, T.J. Park, Cu-nanoflower decorated gold nanoparticles-graphene oxide nanofiber as electrochemical biosensor for glucose detection, Mater. Sci. Eng. C 107 (2020) 110273.
[9] O. Jalil, C.M. Pandey, D. Kumar, Electrochemical biosensor for the epithelial cancer biomarker EpCAM based on reduced graphene oxide modified with nanostructured titanium dioxide, Microchim. Acta 187 (2020) 275.
[10] M. Balamurugan, P. Santharaman, T. Madasamy, S. Rajesh, N.K. Sethy, K. Bhargava, S. Kotamraju, C. Karunakaran, Recent trends in electrochemical biosensors of superoxide dismutases, Biosens. Bioelectron. 116 (2018) 89–99.
[11] X. Tan, L. Ma, P. Han, H. Wei, Q. Wei, C. Sun, Fabrication of boron-doped diamond films electrode for efficient electrocatalytic degradation of cresols, Chemosphere 246 (2020) 125786.
[12] R.B. Phillips, R.R. James, M.L. Magnuson, Electrolyte selection and microbial toxicity for electrochemical oxidative water treatment using a boron-doped diamond anode to support site specific contamination incident response, Chemosphere 197 (2018) 135–141.
[13] D. Banerjee, K.J. Sankaran, S. Deshmukh, M. Ficek, G. Bhattacharya, J. Ryl, D.M. Phase, M. Gupta, R. Bogdanowicz, I.N. Lin, A. Kanjilal, K. Haenen, S.S. Roy, 3D hierarchical boron-doped diamond-multilayered graphene nanowalls as an efficient supercapacitor electrode, J. Phys. Chem. C 123 (2019) 15458–15466.
[14] X.R. Mei, Q.P. Wei, H.Y. Long, Z.M. Yu, Z.J. Deng, L.C. Meng, J. Wang, J.T. Luo, C.T. Lin, L. Ma, K.Z. Zheng, N.X. Hu, Long-term stability of Au nanoparticle-anchored porous boron-doped diamond hybrid electrode for enhanced dopamine detection, Electrochim. Acta 271 (2018) 84–91.

[15] T. Matsubara, M. Ujie, T. Yamamoto, Y. Einaga, T. Daidoji, T. Nakaya, T. Sato, Avian influenza virus detection by optimized peptide termination on a boron-doped diamond electrode, ACS Sens. 5 (2020) 431–439.
[16] V.Y. Maldonado, P.J. Espinoza-Montero, C.A. Rusinek, G.M. Swain, Analysis of Ag(I) biocide in water samples using anodic stripping voltammetry with a boron-doped diamond disk electrode, Anal. Chem. 90 (2018) 6477–6485.
[17] M. Sobaszek, K. Siuzdak, J. Ryl, R. Bogdanowicz, G.M. Swain, The electrochemical determination of isatin at nanocrystalline boron-doped diamond electrodes: stress monitoring of animals, Sensor. Actuator. B Chem. 306 (2020) 127592.
[18] R.G. Rocha, W.P. Silva, R.M.F. Sousa, M.C. Junior, M.H.P. Santana, R.A.A. Munoz, E.M. Richter, Investigation of midazolam electro-oxidation on boron doped diamond electrode by voltammetric techniques and density functional theory calculations: application in beverage samples, Talanta 207 (2020) 120319.
[19] Z. Gong, N. Hu, W. Ye, K. Zheng, C. Li, L. Ma, Q. Wei, Z. Yu, K. Zhou, N. Huang, C.-T. Lin, J. Luo, High-performance non-enzymatic glucose sensor based on Ni/Cu/boron-doped diamond electrode, J. Electroanal. Chem. 841 (2019) 135–141.
[20] Z. Feng, N. Gao, J. Liu, H. Li, Boron-doped diamond electrochemical aptasensors for trace aflatoxin B1 detection, Anal. Chim. Acta 1122 (2020) 70–75.
[21] M.A. Komkova, A. Pasquarelli, E.A. Andreev, A.A. Galushin, A.A. Karyakin, Prussian Blue modified boron-doped diamond interfaces for advanced H_2O_2 electrochemical sensors, Electrochim. Acta 339 (2020) 135924.
[22] X.X. Yuan, N. Gao, X. Gao, D.C. Qiu, R. Xu, Z.L. Sun, Z.G. Jiang, J.S. Liu, H.D. Li, Nanopyramid boron-doped diamond electrode realizing nanomolar detection limit of 4-nonylphenol, Sensor. Actuator. B Chem. 281 (2019) 830–836.
[23] W. Dai, H. Li, M. Li, C. Li, X. Wu, B. Yang, Electrochemical imprinted polycrystalline nickel-nickel oxide half-nanotube-modified boron-doped diamond electrode for the detection of l-serine, ACS Appl. Mater. Interfaces 7 (2015) 22858–22867.
[24] W. Dai, M. Li, H. Li, B. Yang, Amperometric biosensor based on nanoporous nickel/boron-doped diamond film for electroanalysis of l-alanine, Sensor. Actuator. B Chem. 201 (2014) 31–36.
[25] Z.L. Liu, H.J. Li, M.J. Li, C.P. Li, L.R. Qian, L. Su, B.H. Yang, Preparation of polycrystalline BDD/Ta electrodes for electrochemical oxidation of organic matter, Electrochim. Acta 290 (2018) 109–117.
[26] H.J. Li, J.Q. Qin, M.J. Li, C.P. Li, S. Xu, L.R. Qian, B.H. Yang, Gold-nanoparticle-decorated boron-doped graphene/BDD electrode for tumor marker sensor, Sensor. Actuator. B Chem. 302 (2020) 127209.
[27] Y. Li, H. Li, M. Li, C. Li, D. Sun, B. Yang, Porous boron-doped diamond electrode for detection of dopamine and pyridoxine in human serum, Electrochim. Acta 258 (2017) 744–753.
[28] W. Dai, M. Li, S. Gao, H. Li, C. Li, S. Xu, X. Wu, B. Yang, Fabrication of Nickel/nanodiamond/boron-doped diamond electrode for non-enzymatic glucose biosensor, Electrochim. Acta 187 (2016) 413–421.
[29] P. Yu, J. Zhang, T. Zheng, T. Wang, Influence of boron doped level on the electrochemical behavior of boron doped diamond electrodes and uric acid detection, Colloid. Surface. Physicochem. Eng. Aspect. 494 (2016) 241–247.
[30] T. Watanabe, S. Yoshioka, T. Yamamoto, H. Sepehri-Amin, T. Ohkubo, S. Matsumura, Y. Einaga, The local structure in heavily boron-doped diamond and the effect this has on its electrochemical properties, Carbon 137 (2018) 333–342.
[31] P. Kuang, K. Natsui, C. Feng, Y. Einaga, Electrochemical reduction of nitrate on boron-doped diamond electrodes: effects of surface termination and boron-doping level, Chemosphere 251 (2020) 126364.
[32] J. Xu, K. Natsui, S. Naoi, K. Nakata, Y. Einaga, Effect of doping level on the electrochemical reduction of CO_2 on boron-doped diamond electrodes, Diam. Relat. Mater. 86 (2018) 167–172.
[33] S.P. Selvam, M. Hansa, K. Yun, Simultaneous differential pulse voltammetric detection of uric acid and melatonin based on a self-assembled Au nanoparticle–MoS_2 nanoflake sensing platform, Sensor. Actuator. B Chem. 307 (2020) 127683.
[34] E. Castagnola, K. Woeppel, A. Golabchi, M. McGuier, N. Chodapaneedi, J. Metro, I.M. Taylor, X.T. Cui, Electrochemical detection of exogenously administered melatonin in the brain, Analyst 145 (2020) 2612–2620.
[35] S. Yang, J. Zhao, S. Tricard, L. Yu, J. Fang, A sensitive and selective electrochemical sensor based on N, P-Doped molybdenum Carbide@Carbon/Prussian blue/graphite felt composite electrode for the detection of dopamine, Anal. Chim. Acta 1094 (2020) 80–89.
[36] Z.J. Ayres, J.C. Newland, M.E. Newton, S. Mandal, O.A. Williams, J.V. Macpherson, Impact of chemical vapour deposition plasma inhomogeneity on the spatial variation of sp^2 carbon in boron doped diamond electrodes, Carbon 121 (2017) 434–442.
[37] Z.J. Ayres, A.J. Borrill, J.C. Newland, M.E. Newton, J.V. Macpherson, Controlled sp^2 functionalization of boron doped diamond as a route for the fabrication of robust and nernstian pH electrodes, Anal. Chem. 88 (2016) 974–980.
[38] J.V. Macpherson, A practical guide to using boron doped diamond in electrochemical research, Phys. Chem. Chem. Phys. 17 (2015) 2935–2949.
[39] R. Sukanya, S. Ramki, S.M. Chen, R. Karthik, Ultrasound treated cerium oxide/tin oxide (CeO_2/SnO_2) nanocatalyst: a feasible approach and enhanced electrode material for sensing of anti-inflammatory drug 5-aminosalicylic acid in biological samples, Anal. Chim. Acta 1096 (2020) 76–88.
[40] G.Y. Lee, J.H. Park, Y.W. Chang, S. Cho, M.J. Kang, J.C. Pyun, Redox cycling-based immunoassay for detection of carcinogenic embryonic antigen, Anal. Chim. Acta 971 (2017) 33–39.
[41] R. Sakthivel, S. Kubendhiran, S.-M. Chen, J.V. Kumar, Rational design and facile synthesis of binary metal sulfides VS_2-SnS_2 hybrid with functionalized multiwalled carbon nanotube for the selective detection of neurotransmitter dopamine, Anal. Chim. Acta 1071 (2019) 98–108.
[42] X. Sun, L. Zhang, X. Zhang, X. Liu, J. Jian, D. Kong, D. Zeng, H. Yuan, S. Feng, Electrochemical dopamine sensor based on superionic conducting potassium ferrite, Biosens. Bioelectron. 153 (2020) 112045.
[43] N. Roy, S. Yasmin, S. Jeon, Effective electrochemical detection of dopamine with highly active molybdenum oxide nanoparticles decorated on 2, 6 diaminopyridine/reduced graphene oxide, Microchem. J. 153 (2020) 104501.
[44] K. Tyszczuk-Rotko, I. Jaworska, K. Jedruchniewicz, Application of unmodified boron-doped diamond electrode for determination of dopamine and paracetamol, Microchem. J. 146 (2019) 664–672.
[45] N. Soltani, N. Tavakkoli, F. Shahdost-Fard, H. Salavati, F. Abdoli, A carbon paste electrode modified with Al_2O_3-supported palladium nanoparticles for simultaneous voltammetric determination of melatonin, dopamine, and acetaminophen, Microchim. Acta 186 (2019) 540.
[46] C. Dincer, R. Ktaich, E. Laubender, J.J. Hees, J. Kieninger, C.E. Nebel, J. Heinze, G.A. Urban, Nanocrystalline boron-doped diamond nanoelectrode arrays for ultrasensitive dopamine detection, Electrochim. Acta 185 (2015) 101–106.
[47] H. Zeinali, H. Bagheri, Z. Monsef-Khoshhesab, H. Khoshsafar, A. Hajian, Nanomolar simultaneous determination of tryptophan and melatonin by a new ionic liquid carbon paste electrode modified with SnO_2-Co_3O_4@rGO nanocomposite, Mater. Sci. Eng. C 71 (2017) 386–394.
[48] N. Kumar, Rosy, R.N. Goyal, Nanopalladium grained polymer nanocomposite based sensor for the sensitive determination of Melatonin, Electrochim. Acta 211 (2016) 18–26.